

Trace Amount of Water Boosting Highly Selective Coupling of Methane to Ethane via a Noble-Metal Free Ni²⁺-doped MgO/Al₂O₃ Photocatalyst

Yu-Fei Song (✉ songyf@mail.buct.edu.cn)

Beijing University of Chemical Technology

Tianyang Shen

Beijing University of Chemical Technology

Ya Bai

Beijing University of Chemical Technology

Zelin Wang

Beijing University of Chemical Technology

Xiaoliang Sun

Beijing University of Chemical Technology

Guihao Liu

Beijing University of Chemical Technology

Sha Bai

State Key Laboratory of Chemical Resource Engineering, Beijing University of Chemical Technology

Jiixin Li

Beijing University of Chemical Technology

Lirong Zheng

Beijing Synchrotron Radiation Facility, Institute of High Energy Physics, Chinese Academy of Sciences

Article

Keywords: Photocatalysis, Methane coupling reaction, Topotactic conversion, Layered double hydroxides

Posted Date: May 24th, 2022

DOI: <https://doi.org/10.21203/rs.3.rs-1663512/v1>

License:  This work is licensed under a Creative Commons Attribution 4.0 International License.

[Read Full License](#)

Trace Amount of Water Boosting Highly Selective Coupling of Methane to Ethane via a Noble-Metal Free Ni²⁺-doped MgO/Al₂O₃ Photocatalyst

Tianyang Shen^{1,†}, Ya Bai^{1,†}, Zelin Wang¹, Xiaoliang Sun¹, Guihao Liu¹, Sha Bai¹, Jiabin Li¹, Lirong Zheng^{2,*} and Yu-Fei Song^{1,*}

¹State Key Laboratory of Chemical Resource Engineering, Beijing Advanced Innovation Centre for Soft Matter Science and Engineering, Beijing University of Chemical Technology, Beijing 100029, P. R. China. Email: songyf@mail.buct.edu.cn.

²Beijing Synchrotron Radiation Facility, Institute of High Energy Physics, Chinese Academy of Sciences, Beijing 100049, P. R. China. Email: zhenglr@ihep.ac.cn.

[†]These authors contributed equally to this work

Abstract: Direct and selective coupling of methane into high-value added products under mild conditions is a grand challenge since the activation of the inert C-H bonds (439 kJ mol⁻¹) and the inhibition of over-oxidation are simultaneously required. Herein, we report the fabrication of a noble-metal free Ni²⁺-doped MgO/Al₂O₃ photocatalyst (NiMgAl-x, x represents calcination temperature) through facile topotactic conversion of the corresponding NiMgAl-layered double hydroxides (denoted as NiMgAl-LDH). EXAFS spectroscopy demonstrates that for NiMgAl-x, the Ni²⁺ ions are isomorphically doped into MgO cell and no NiO phase is formed. By involving trace amounts of water, photo-oxidation of methane to ethane can be accomplished by using NiMgAl-800 as catalyst in a flow reactor with a high production rate (454.30 μmol g⁻¹ h⁻¹) and a superior selectivity (97.8%), which was the highest yield among all the noble-metal free photocatalysts reported so far. Detailed characterizations reveal the electron-enriched surface oxygens of NiMgAl-800 generated during the topotactic process lead to the enhanced photocatalytic activity. In-situ DRIFT experiments and DFT calculations show that the introduced H₂O molecules can modulate the Gibbs free energy of •CH₃ towards a coupling conductive pathway instead of production of CO₂, resulting in an increased C₂H₆ selectivity and inhibited CO₂ production.

Keywords: Photocatalysis, Methane coupling reaction, Topotactic conversion, Layered double hydroxides

Introduction

Methane, the main component of the natural gas, flammable ice and shale gas, is playing an increasingly important role in the energy industry^{1,2}. Currently, the majority of methane is burned directly for the purpose of heating, transportation and power generation, making it the world's second largest source of greenhouse gases³. It's worthwhile noting that methane is also a vital block for fabricating value-added high-carbon products⁴. At present, the industrialized process is the steam / dry reforming of methane, which firstly cracks methane into syngas (CO and H₂) and then converts it into high-carbon products through the Fischer-Tropsch reaction⁵. Large amounts of energy are required in the above-mentioned process due to the high reaction temperature (>700 °C) and the indirect conversion of methane⁶. To develop an economical and environment-friendly substitution, it's highly desirable to accomplish the direct conversion of methane into high-carbon products under mild conditions⁷⁻⁹. Nevertheless, the inherent properties of methane such as the low polarizability, negligible electron affinity, and strong C-H binding energy (439 kJ mol⁻¹) makes the direct activation of methane highly challenging¹⁰⁻¹³. From a thermodynamic perspective, once the methane is activated, the produced •CH₃ radicals tend to generate the over-oxidative product CO or CO₂¹⁴. Hence, the key for methane activation under mild conditions is to fabricate efficient catalysts with both high activity and selectivity.

It's widely recognized that the rate-determine step in methane activation is the cleavage of the first C-H bond¹⁵. Bao and his coworkers proposed two kinds of methane activation sites: unsaturated coordinative metal sites and reactive oxygen sites^{15, 16}. The utilization of unsaturated coordinative metal sites commonly requires the participation of precious metals (Au, Pd, et al.)¹⁷⁻²⁰. For example, Ye and her coworkers presented the coupling of methane to ethane with the production rate of 5020 μmol g⁻¹ h⁻¹ by using noble-metal photocatalyst of Au-ZnO/TiO₂²¹, which is the highest yield reported so far in the literature. Considering the cost and scarcity of these noble-metals, it's worthwhile to develop noble-metal free photocatalyst to active methane directly²².

The reactive oxygen sites are mainly composed of electrophilic oxygen atoms on the catalysts surface, such as metal-oxide (M-O) sites on ZnO, TiO₂, MgO, etc. Compared with ZnO and TiO₂, MgO was demonstrated to be able to activate methane under thermal catalysis conditions but rarely investigated in photocatalysis^{23, 24}. In the meanwhile, photocatalytic process is able to generate photo-electrons to maintain up-hill reactions, which is able to avoid thermodynamic limitations and

hopeful to produce high-carbon products²⁵. Layered double hydroxides (denoted as LDH)²⁷⁻²⁹, in which the divalent metals are evenly dispersed on the LDH laminate^{30, 31}, are a class of ideal precursors to fabricate highly dispersed metal oxides through topotactic conversion process.^{32, 33} Moreover, the Ni²⁺ ions are likely to isomorphically doped into MgO cell during the calcinating process of NiMgAl-LDH, and thereby adjust the energy density of oxygen²⁶.

Herein, the Ni-doped MgO nanosheets were successfully synthesized through topotactic transformation of NiMgAl-LDH from 200 °C to 1000 °C, the as-prepared catalysts were denoted as NiMgAl-x. Interestingly, we found the electronic state of surface oxygen species can be finely tuned during the topotactic process. The coordinative structure of NiMgAl-x was finely investigated by XANES and EXAFS analysis. In the photocatalytic methane coupling experiment, a high production rate (454.30 $\mu\text{mol g}^{-1} \text{h}^{-1}$) and a superior selectivity (97.8%) for ethane was achieved in a gas flow reactor. Moreover, we found the productivity and selectivity can be significantly improved by involving trace amounts of water. Detailed catalytic process was carefully investigated by using in-situ DRIFT and DFT calculation.

Results and discussions

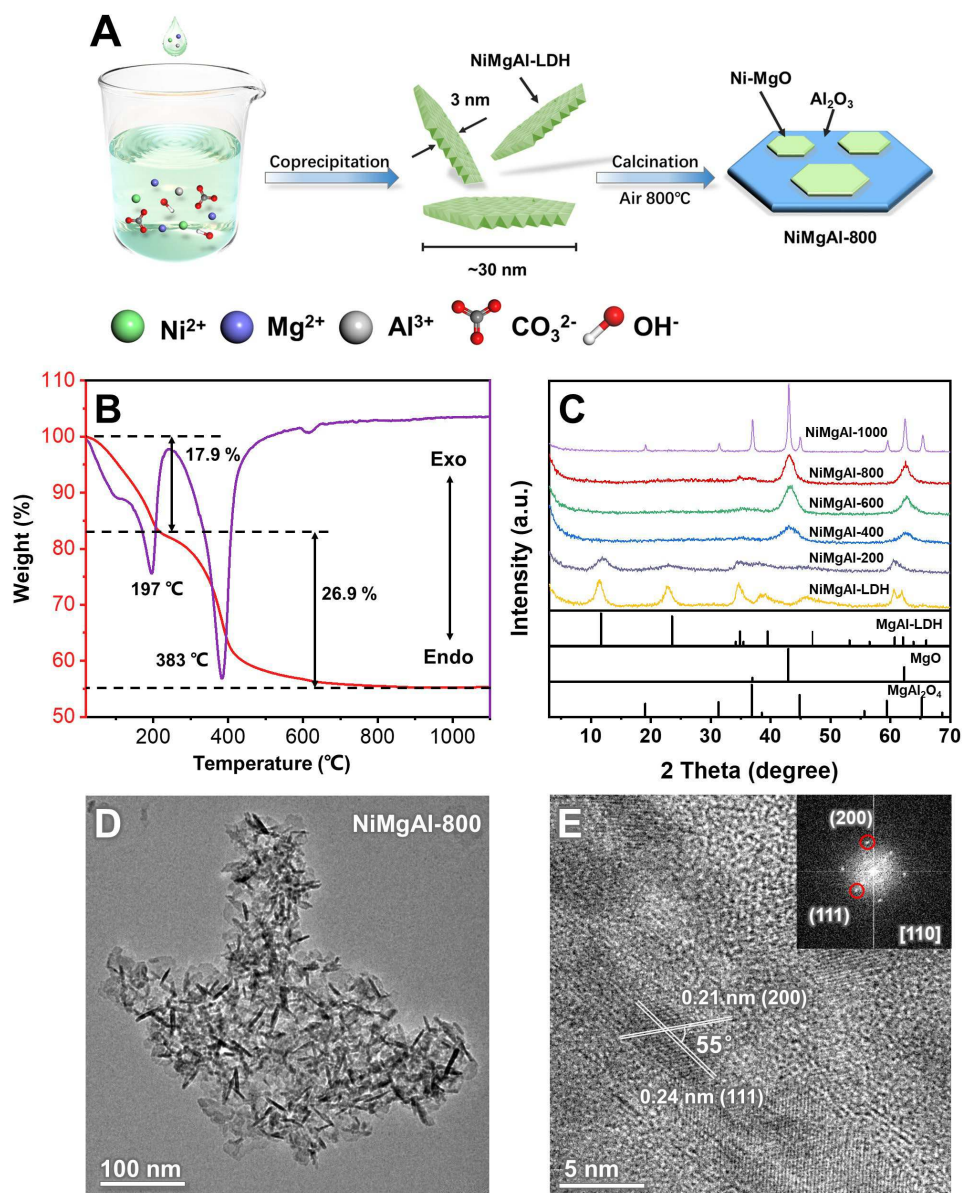


Figure 1. The synthesis process and basic structure of NiMgAl-x. A) Schematic illustration of the synthesis procedure for NiMgAl-x. B) The thermogravimetric-differential thermal analysis (TG-DTA) of NiMgAl-800. C) XRD patterns of NiMgAl-x. D) The TEM image of NiMgAl-800. E) The HRTEM image of NiMgAl-800 and corresponding FFT pattern.

Firstly, the NiMgAl-LDHs was synthesized through a classic co-precipitation method³⁴, in which the nickel content is 5% in molar ratio. Afterwards, the as-prepared LDH was calcinated in air from 200 °C to 1000 °C to obtain the corresponding NiMgAl-x (Figure 1A). TG-DTA analysis was performed to detect the weight loss during the topotactic transformation process (Figure 1B). The first weight-loss ranging from 30 to 200 °C was assigned to the loss of H_2O molecules adsorbed

on the LDH laminate and intercalated between the LDH layers³⁵. The second stage in the range of 300 to 500 °C can be corresponded to the loss of interlayered carbonates. Meanwhile, the powder X-ray diffraction (XRD) analysis was conducted to detect the basic structure of each state during the calcination process. As shown in Figure 1C, the typical (00 l) and (110) basal reflection peak of NiMgAl-LDH, demonstrated that the LDH precursor was synthesized successfully³⁶. The (003) peak shifted from 11.4° to 12.0° in NiMgAl-200, suggesting a reduced layer spacing, which was attributed to the release of intercalated water³⁷. The characteristic reflection peak of MgO can be observed in NiMgAl-400 while no feature of NiO or Al₂O₃ can be detected, indicating that the NiMgAl-LDH was topotactically transformed to MgO and amorphous Al₂O₃ phase. With the raise of the calcination temperature from 400 °C to 800 °C, the intensity of MgO phase increased accordingly, suggesting an improved crystallinity³⁷. As the calcination temperature reached 1000 °C, the NiMgAl-1000 transformed into the corresponding MgAl₂O₄ structure.

The transmission electron microscopy (TEM) and high-resolution transmission electron microscopy (HRTEM) measurement were conducted to follow the morphology change during the calcination process (Figure S1). In Figure S1A-B, the NiMgAl-LDH and NiMgAl-200 presented a typical layered structure. With the increase of the calcination temperature, the NiMgAl-x maintained its layered structure throughout the calcination process with the lateral size of ~30 nm and the thickness of ~3.5 nm. And this layered structure brings a larger specific area for NiMgAl-800 than commercial MgO (Figure S2). In the case of NiMgAl-800, the lattice fringe spacing of 0.21 nm and 0.24 nm can be assigned to the (200) and (111) facet of MgO, respectively (Figure 1E). And the interfacial angle of 55° between these two lattice fringes indicated that the NiMgAl-800 nanosheets are dominated by exposed {110} facet of MgO. Meanwhile, the NiMgAl-800 presented a light green color (Figure S1F), which facilitated its light absorption in the ultraviolet and visible wavelengths (Figure S3).

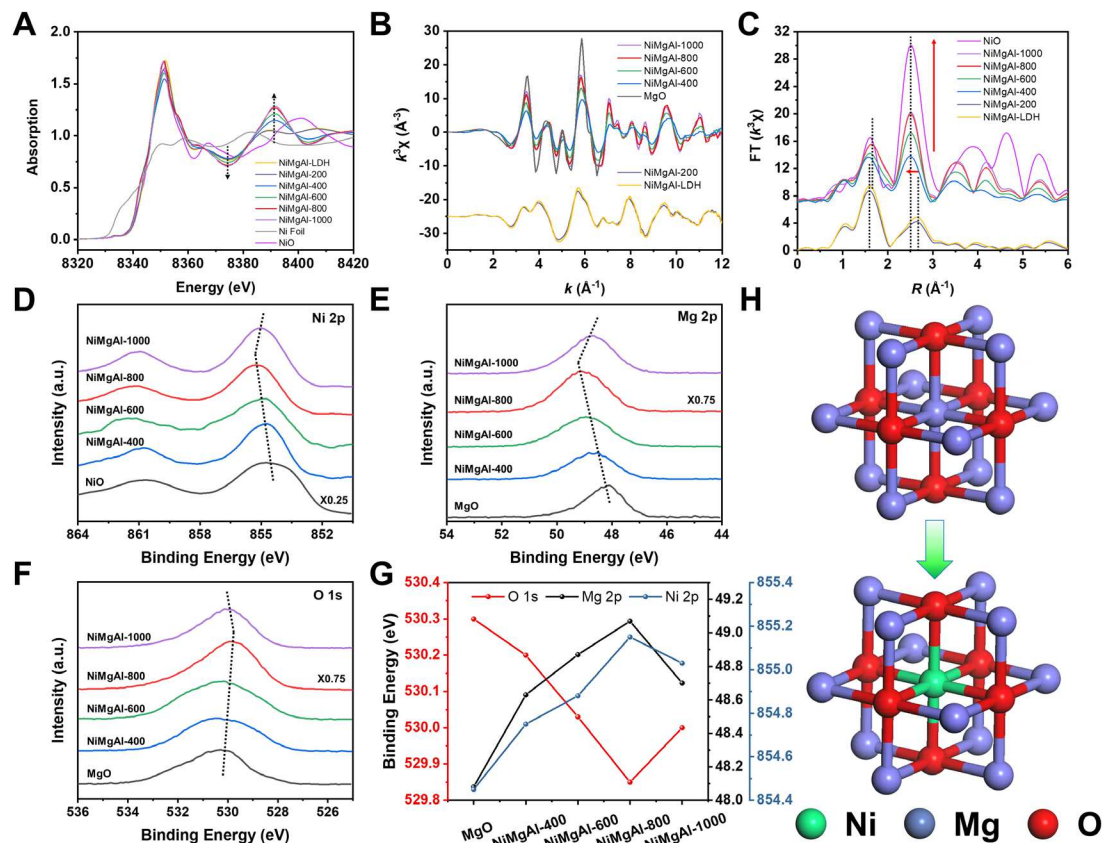


Figure 2. Fine structure characterization and electronic states of NiMgAl-x. A-C) Ni k-edge $k^3 \chi(k)$ oscillation spectra for NiMgAl-x and NiO and its corresponding K space and R space data. D-F). XPS data of Ni 2p, Mg 2p, O 1s orbital and their corresponding changes in binding energy were presented in figure 2G. H) The schematic illustration of the MgO structure model and Ni-MgO model in the corresponding NiMgAl-800.

To further reveal the local environment of the Ni species, the X-ray adsorption fine structure (XAFS) spectroscopy was used to detect the fine coordination structure of NiMgAl-x. As shown in Figure 2A, the oscillation of NiMgAl-x in Ni k-edge XANES was completely different from Ni foil and the reference NiO, suggesting that the different local coordination environment of the Ni²⁺ ions. From the k space plot (Figure 2B), the NiMgAl-200 exhibited similar oscillation spectra to that of NiMgAl-LDH, indicating the LDH maintained its structure at 200 °C, which was in consistent with the XRD result. When the calcination temperature reached 400 °C, the NiMgAl-x presented a totally different oscillation spectrum, illustrating that the NiMgAl-LDH was converted into the corresponding metal oxide. Furthermore, the Ni k space XANES of the NiMgAl-800 exhibited similar oscillation to the reference MgO rather than NiO (Figure 2B and Figure S4), indicating that the Ni²⁺ ions were isomorphically doped into the MgO unit cell and occupied the position of Mg²⁺

ions. In the R space spectrum (Figure 2C), the first peak and the second peak was corresponded to Ni-O shell and Ni-M shell (M was short for metal), respectively. On the basis of the extended XAFS (EXAFS) fitting results (Figure S5 and Table S1), with the raise of the calcination temperature, the coordination number (N) of the Ni^{2+} ions increased accordingly, and the NiMgAl-800 exhibited the highest coordination number in both Ni-O shell (4.98) and Ni-M shell (11.05). Furthermore, the Debye-Waller factor of NiMgAl-800 for both shells was lowest ($4.55 \times 10^{-3} \text{ \AA}^2$ and $6.00 \times 10^{-3} \text{ \AA}^2$, respectively), suggesting the structural distortion surrounded Ni^{2+} ions in NiMgAl-800 reached the lowest level compared with other calcination products. Meanwhile, in the wavelet transform (WT) analysis of EXAFS (Figure S6), the intensity maximum region around $6\sim 8 \text{ k \AA}^{-1}$, $2\sim 3 \text{ R} + \alpha \text{ \AA}$ can be corresponded to the Ni-M shell. The position of Ni-M shell in NiMgAl- x was around 6.1 \AA , which was much smaller than that in NiO reference (around 8.1 \AA), demonstrating that Ni^{2+} ions in NiMgAl- x were mostly surrounded by Mg^{2+} ions rather than Ni^{2+} ions. Consequently, the structural illustration of NiMgAl-800 was presented in Figure 2H.

Additionally, the surface electronic states of O species can be finely controlled during the calcination process. Derived from the X-ray photoelectron spectroscopy (XPS) results (Figure 2D-F), as the calcination temperature increased, the binding energy of Ni^{2+} and Mg^{2+} ions increased and reached the highest level at $800 \text{ }^\circ\text{C}$, whereas the binding energy of O presented a rapid decrease, and reached the lowest value at $800 \text{ }^\circ\text{C}$. The change in binding energy of each element were summarized in Figure 2G, exhibiting the electron was transferred from Ni^{2+} and Mg^{2+} to $\text{O}^{-(2+\delta)}$ during the calcination process. The NiMgAl-800 showed the lowest valance state of $\text{O}^{-(2+\delta)}$ ($\delta > 0$) among all the calcination samples of NiMgAl- x ($x=400, 600, 800, 1000$).

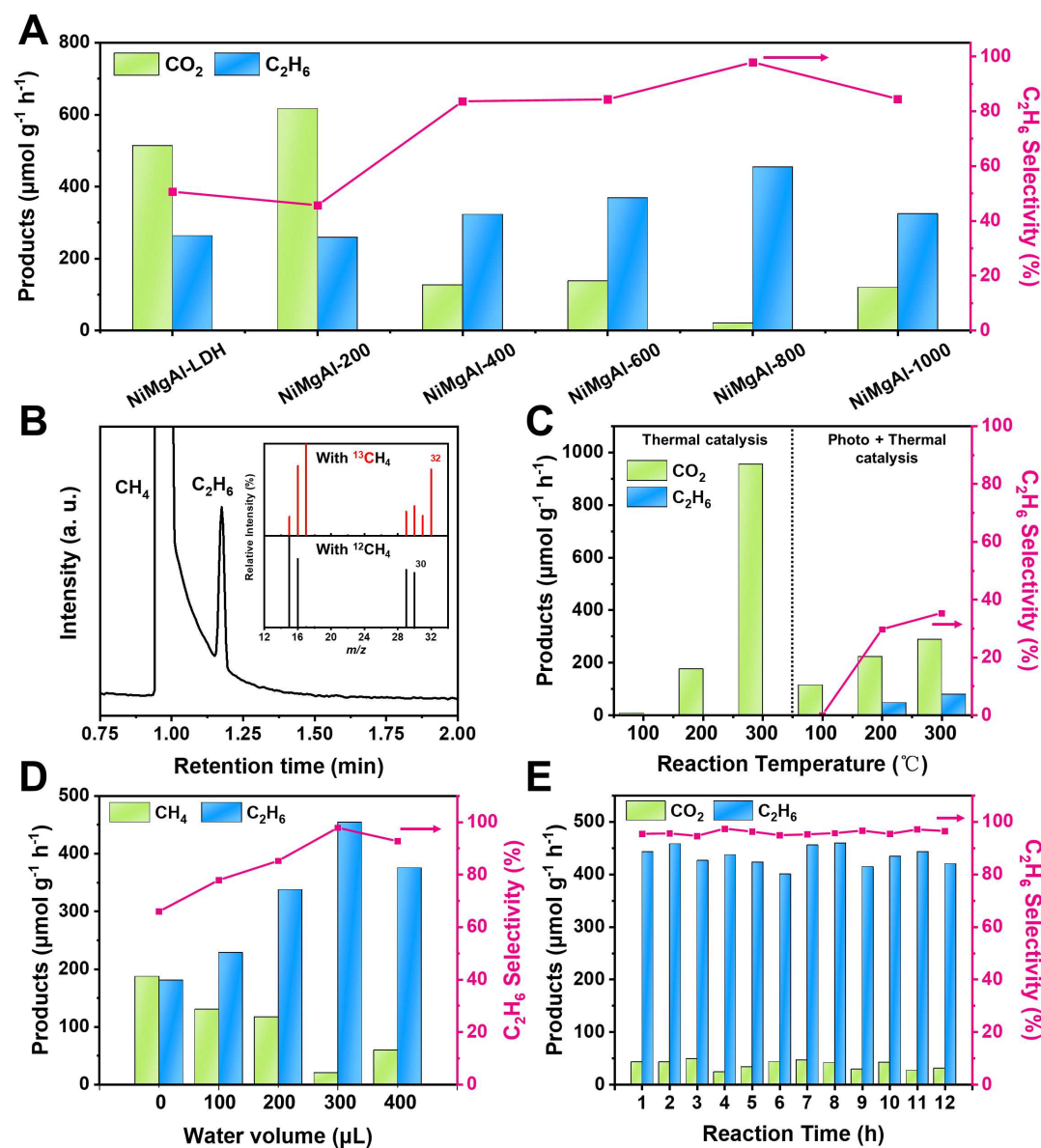


Figure 3. The photocatalytic performance of NiMgAl-x. Comparison of the photocatalytic methane coupling activity over NiMgAl-x. B) GC-MS results of C₂H₆ products originated from ¹²CH₄ and ¹³CH₄ isotope experiments of NiMgAl-800. C) Photocatalytic methane coupling activity of NiMgAl-800 with different volume of water addition. D) Photocatalytic methane coupling activity at evaluated temperatures under dark (thermal catalysis) or light (400-800 nm) irradiation (Photo + Thermal catalysis) conditions. E) Stability evaluation of photocatalytic methane coupling activity over NiMgAl-800 in 12h. Reaction condition: 5 mg catalyst, 300 μL water, 20 mL min⁻¹ CH₄ and 300 W Xe lamp full spectrum light irradiation.

Since the NiMgAl-x was successfully synthesized through the fine tuning of the calcination temperature, the photocatalytic methane activation experiment was conducted to evaluate its

catalytic performance. The as-prepared photocatalysts were tested under 300 W Xe lamp irradiation and 20 mL min⁻¹ CH₄ for 3 h in a flow reactor (Figure S7), the amount of catalyst and water was 5 mg and 300 μL in each experiment, respectively. In Figure 3 A, the production rate for C₂H₆ exhibited a volcano-like trend as follows: NiMgAl-LDH (263.3 μmol g⁻¹ h⁻¹) ≈ NiMgAl-200 (259.0 μmol g⁻¹ h⁻¹) < NiMgAl-400 (322.4 μmol g⁻¹ h⁻¹) < NiMgAl-600 (368.9 μmol g⁻¹ h⁻¹) < NiMgAl-1000 (324.1 μmol g⁻¹ h⁻¹) < NiMgAl-800 (454.3 μmol g⁻¹ h⁻¹). NiMgAl-800 presented the highest C₂H₆ selectivity of 97.8% and production rate of 454.3 μmol g⁻¹ h⁻¹ among all calcination products. Moreover, the over-oxidative product CO₂ can be mostly suppressed at the same time (selectivity 2.2%) (Figure S8). No liquid product was detected throughout the photocatalytic process. It was noteworthy that the binding energy of oxygen in NiMgAl-x (x=400, 600, 800, 1000) presented a similar tendency, indicating that the oxidative state of O has strong relationship with the selectivity for C₂H₆. Importantly, to the best of our knowledge, this catalytic performance was the highest yield among all the reported non-precious metal photocatalysts so far and was better than most other noble metal based photocatalysts in the lately reported works (Table S2). Additionally, the activity of each single component MgO, Al₂O₃ and NiO was evaluated (Figure S9). MgO presented a satisfactory C₂H₆ selectivity (84.3%) but a relative low production rate (279.3 μmol g⁻¹ h⁻¹). On the contrary, NiO exhibited a better reactivity but a lower selectivity for C₂H₆. Moreover, the performance of physically mixed MgO, Al₂O₃ and NiO was poor in both selectivity and production rate for C₂H₆, which further confirming the significance of the electron-enriched oxygen in NiMgAl-800 for promoting the photocatalytic methane coupling reactivity. The flow rate of methane was also been modulated in Figure S10, the increase of methane flow rate from 5 mL min⁻¹ to 20 mL min⁻¹ led to a higher ethane selectivity and a little decrease in ethane yield, which was in good consistent with the reported literature³⁸.

Furthermore, the ¹³CH₄ isotopic labeling experiment (Figure 3B) demonstrated that the produced C₂H₆ was derived from ¹²CH₄. In Figure S11, the photocatalytic activity of NiMgAl-800 over reaction time was recorded, the production rate and selectivity for ethane can be continuously maintained above 420 μmol g⁻¹ h⁻¹ and 95%, respectively. In the 12 h continuous stability test (Figure 3E), there was no obvious decrease in selectivity and production rate, illustrating that the excellent stability of NiMgAl-800. The XRD pattern (Figure S12) of NiMgAl-800 after reaction displayed no distinct difference from its initial form, which further demonstrated the catalyst

structure remained unchanged over at least 12 hours. Moreover, from the Raman spectroscopy (Figure S13), the intensity around two coke bands (1400 cm^{-1} and 1600 cm^{-1})²² were negligible, indicating the NiMgAl-800 presented excellent coke-resistance. In the optoelectronic test (Figure S14 -15), NiMgAl-800 both exhibit minimized charge-transfer resistance, best photoelectric response and electrochemical specific area among all the calcination products. Indicating the transfer of photo-generated electrons in NiMgAl-800 was most efficient, which well-explained the reason why NiMgAl-800 possess higher C_2H_6 productivity.

The photo-thermal effect of NiMgAl-800 was also taken into consideration. The surface temperature of the photocatalysts was valued by an electric temperature probe (Figure S16), which rise sharply to $130\text{ }^\circ\text{C}$ in the first 10 minutes and finally stabilized at $150\text{ }^\circ\text{C}$. In figure 3C, when NiMgAl-800 was treated under dark environment at evaluated temperatures ($100\text{ }^\circ\text{C}$, $200\text{ }^\circ\text{C}$, $300\text{ }^\circ\text{C}$, respectively), only the over-oxidative product CO_2 could be detected (denoted as thermal catalysis). Indicating the coupling reaction was not driven by heat and the methane could not be activated without light irradiation until $200\text{ }^\circ\text{C}$. In the photo-thermal catalysis, the catalysts were treated at the same temperature as thermal catalysis and visible light irradiation ($400\text{-}800\text{ nm}$), CO_2 was the main product and a small amount of C_2H_6 can be detected. The above experiments demonstrated that the photo-energy was the primary driving force for the methane conversion.

Interestingly, there was a very important discovery that trace amount of water ($300\text{ }\mu\text{L}$) played a vital role in the methane coupling reaction (Figure 3D). We used a home-made reactor that separated the catalysts and water by a quartz bowl to prevent the direct contact of catalyst with water (Figure S7). During the reaction process, the water was vaporized and adsorbed on the catalyst surface. Compared with the control experiment without water, the ethane productivity was nearly half-cut and CO_2 can't be suppressed. As the amount of added water increased, the reactivity and selectivity of ethane raised and reached the highest value at $300\text{ }\mu\text{L}$, and the excess involvement of water would decrease of ethane yield. Moreover, the participation of water did not lead to the generation of the oxidative products such as methanol or ethanol in our experiment. To further uncover the mechanism of methane activation and the role of water played in this reaction process, we conducted *quasi-situ* XPS and *in-situ* diffuse reflection infrared fourier transform spectroscopy (*in-situ* DRIFTS) to acquire some mechanistic insights into the methane coupling reaction.

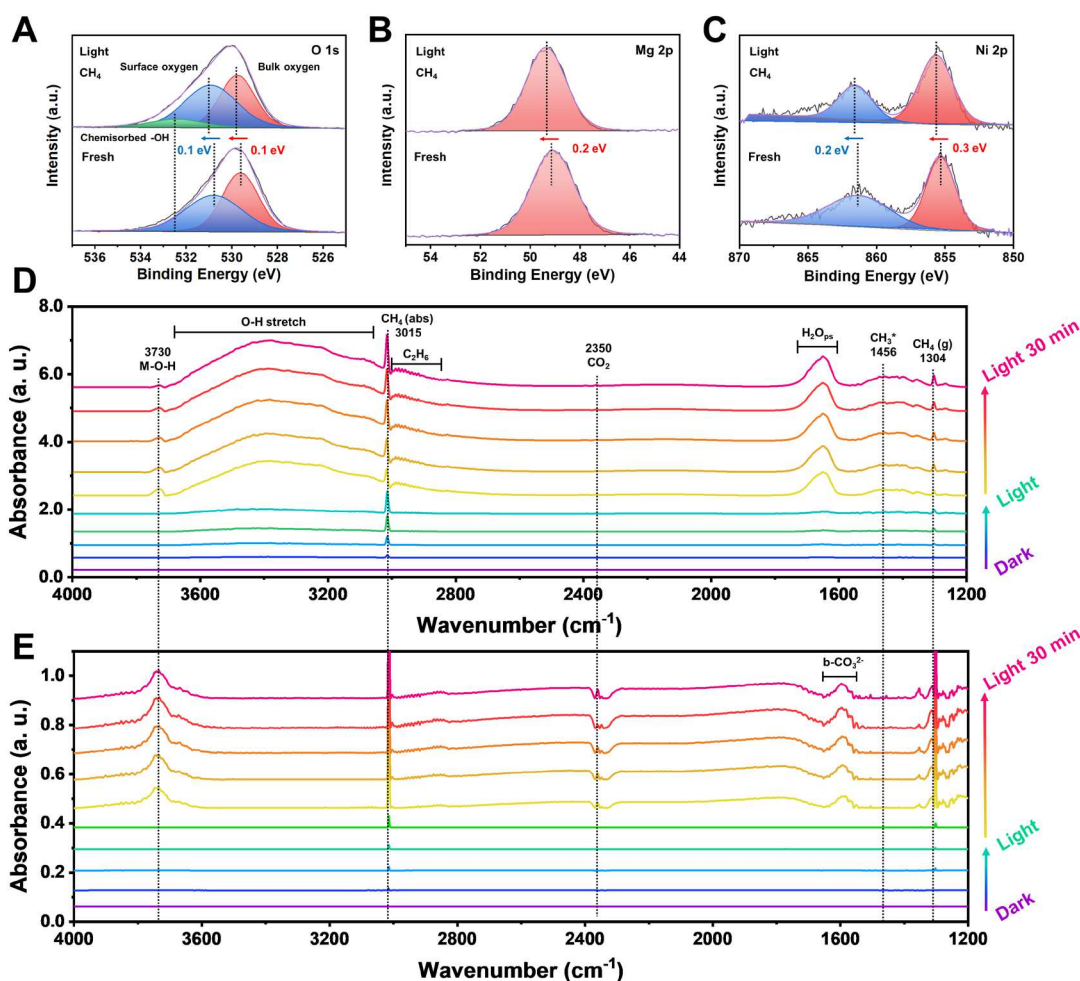


Figure 4. *Quasi-situ* XPS and *in-situ* DRIFT studies of NiMgAl-x. *Quasi-situ* XPS spectra of A) O 1s, B) Mg 1s and C) Ni 2p for NiMgAl-800 after methane coupling reaction in comparison with its initial state. *In-situ* DRIFT spectra of NiMgAl-800 with Xe lamp irradiation under different conditions: D) with water and E) without the treatment of water.

Firstly, the mechanism of methane activation was taken into consideration. The *Quasi-situ* XPS measurements were conducted after treating NiMgAl-800 under light irradiation and 0.1 MPa CH₄ for 3 h with 30 μ L water. According to Figure 4A, the characteristic peaks located at 259.6 eV and 530.8 eV can be ascribed to the bulk oxygen and surface oxygen in NiMgAl-800, respectively³⁹. It was noteworthy that both bulk oxygen and surface oxygen presented a higher binding energy after reaction, indicating the electron transfer during the reaction process. Moreover, there was a new characteristic peak located at 532.4 eV appeared after reaction, which can be corresponded to the chemisorbed hydroxyl species (-OH), illustrating that the methane electrophilic attacked the reactive oxygen sites on NiMgAl-800 and consequently formed the O-H chemical bond. DFT calculation also confirmed this point: the adsorption configuration of CH₄ was on the O-top site with the

adsorption energy of -0.29 eV (Figure 5A). Meanwhile, the quasi-XPS patterns of Mg 2p and Ni 2p were displayed in Figure 4 B-C, both Mg and Ni presented an increase in their valence state after reaction, indicating that the electrons were further transferred to the oxygen sites during the reaction process.

The in-situ DRIFT measurement was another useful method to detect the chemical variation on the surface of NiMgAl-800, which can illustrate the mechanism of methane activation. The NiMgAl-800 was first treated by Ar at 150 °C for 30 minutes in the dark. The background spectra was acquired when the detector was cooled down to 25 °C. In Figure 4D, two sharp peaks located at 1304 cm⁻¹ and 3015 can be corresponded to the CH₄ gas, indicating the methane gas can be captured on the catalyst surface without light irradiation. Soon after, the cell was heated to 150 °C in ten minutes under Xe lamp irradiation to simulate the reaction environment. Once the light was turned on, a new peak can be observed at 3730 cm⁻¹, which was owing to the formation of M-O-H bond. As such, the methane was chemisorbed onto the reactive oxygen sites by O-H bond on the surface of NiMgAl-800. The conclusion was consistent with the *quasi*-XPS measurement and DFT calculation: the electron-enriched oxygen was capable of catching the methane gas and then activated C-H bond by the formation of polarized O-H bond. In the meanwhile, the band located at 1456 cm⁻¹ belonged to the •CH₃ radicals, which was a crucial evidence explaining that the coupling reaction complied with the free radical reaction mechanism. Correspondingly, the broad peak beside the methane gas (2900 cm⁻¹) was the coupling product ethane, demonstrating that a great amount of C₂H₆ was generated under light irradiation.

Successively, the contribution of water was discussed in detail. The *in-situ* DRIFT without water participation was carried out for comparison (Figure 4E). There was a significant difference in this two figures. In Figure 4D, the broad band located at 1635 cm⁻¹ and 3350 cm⁻¹ can be ascribed to the physically adsorbed water (H₂O_{ps}) and stretching vibration of O-H bond, respectively⁴⁰. On the contrary, there was no absorption peak can be observed at the same position in Figure 4F, which further demonstrated that these two unique bands were the contribution of water. Besides, we noticed that without the help of water, the adsorption peak of M-O-H bond located at 3730 cm⁻¹ still appeared, indicating that the NiMgAl-800 can capture methane via the reactive oxygen sites itself. The introduction of water would not affect the activation of methane. However, the band located at 1577 cm⁻¹ in Figure 4F illustrated that the activated methane tended to be over-oxidized to the

carbonates species without water. As a result, the sharp peak located at 2350 cm^{-1} can be corresponded to CO_2 gas, which was in good consistent with the catalytic results, that is, the methane would be over-oxidized to CO_2 without water (Figure 3D). Moreover, it was noteworthy that the intensity of each adsorption peak in Figure 4D was rather higher than that in Figure 4F, indicating the reactivity of NiMgAl-800 was greatly promoted with the participation of water. Therefore, the reactive oxygen sites on the surface of NiMgAl-800 together with the absorbed water presented a synergistic effect to promote the methane activation, resulting in a greatly boosted methane conversion rate. Interestingly, unlike NiMgAl-800, the reference NiO and MgO exhibit negligible adsorption of water (Figure S17) and the by-product CO_2 could not be fully compressed in these two cases.

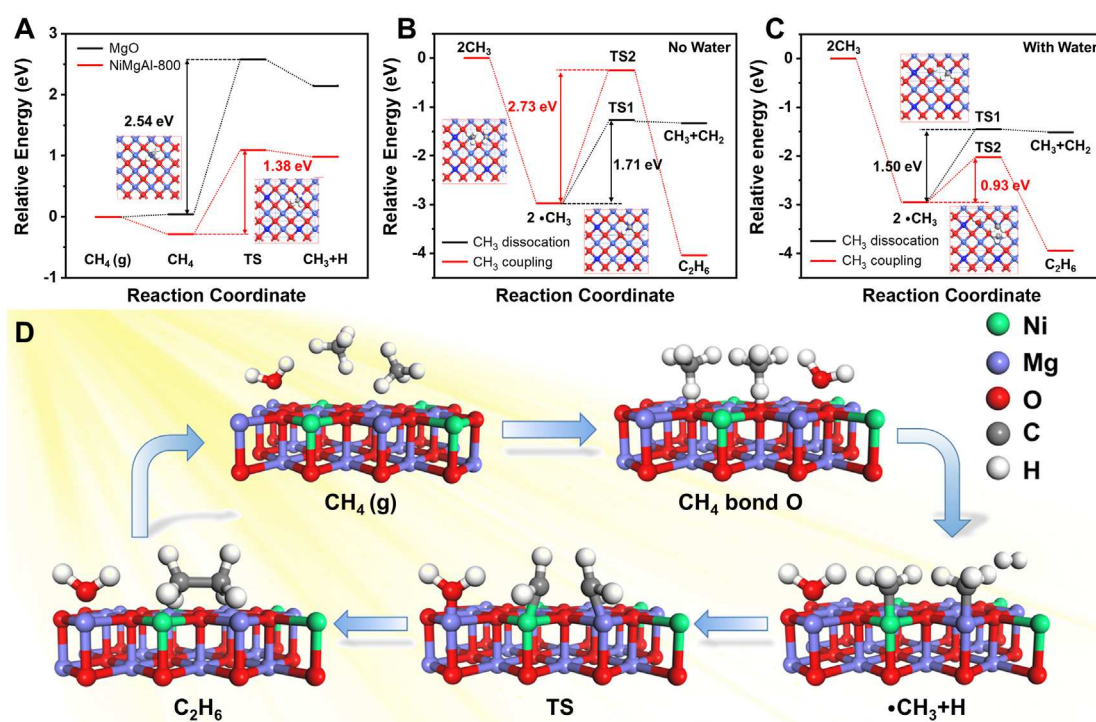


Figure 5. DFT studies. A. Gibbs free energy diagrams of methane activation on NiMgAl-800 and MgO. B-C. Comparison of dissociation and coupling barrier for NiMgAl-800 in Gibbs free energy without water (B) and with water (C). D. Schematic illustration of methane coupling reaction on NiMgAl-800.

To better understand the reaction mechanism of photocatalytic methane coupling reaction, we employed DFT+U calculations to explain such high reactivity of NiMgAl-800 and selectivity to C_2H_6 rather than the over oxidative product CO_2 under light irradiation. Firstly, we compared the Gibbs free energy barriers of methane activation on NiMgAl-800 and MgO. The energy barrier for

the first C-H bond cleavage on NiMgAl-800 was 1.38 eV, which was much lower than that of MgO (2.54 eV). And the generated $\bullet\text{CH}_3$ radicals were more stable on the NiMgAl-800 surface. This result indicated that the Ni doped MgO was more favorable in the methane activation, which was in good line with the experimental results. Next, according to the Figure 5B and C, by comparing the $\bullet\text{CH}_3$ coupling and dissociation mechanisms, we found that the dissociation was more favorable with the lower barrier (1.76 eV) than coupling (2.73 eV) without water. In contrast, after the addition of H_2O , the formation of C_2H_6 through CH_3 coupling showed a barrier of 0.93 eV, which was kinetically more favorable compared with the further dissociation to $\bullet\text{CH}_2$ (1.50 eV). Therefore, the H_2O molecules that adsorbed on the catalyst surface were beneficial for the formation of C_2H_6 , which was in good agreement with our experimental results. Combined with the afore-mentioned experimental and theoretical results, the schematic illustration of the reaction pathway was summarized in Figure 5D. The methane was firstly activated by the electron-enriched oxygen sites on the surface of NiMgAl-800 and formed the O-H bond, the captured C-H bond was then dissociated under light irradiation. The formed $\bullet\text{CH}_3$ species were adsorbed on metal sites (Ni or Mg) with M-C connection. Subsequently, H_2O was adsorbed on an adjacent Mg atom, which promoted the reaction towards a coupling pathway. The generated $\bullet\text{CH}_3$ and $\bullet\text{H}$ intermediates formed a C_2H_6 and H_2 , respectively. Finally, the product ethane and hydrogen were detached from substrate to complete a cycle reaction.

Conclusions

In summary, a series of Ni^{2+} doped $\text{MgO}/\text{Al}_2\text{O}_3$ photocatalysts of NiMgAl-x were successfully fabricated through the topotactic conversion of NiMgAl-LDH. Through XANES and EXAFS analysis, we demonstrated the isomorphic substitution of Mg^{2+} ions by Ni^{2+} ions in MgO cell in the corresponding NiMgAl-x, instead of generating NiO phase. And the WT-EXAFS further illustrated Ni^{2+} ions were mostly surrounded by Mg^{2+} ions in its second coordination shell, indicating the high dispersion of Ni^{2+} ions in NiMgAl-x. More importantly, we found the electronic density of state of surface oxygen species can be finely tuned during the topotactic process. Among NiMgAl-x, the NiMgAl-800 with the most electron-enriched surface oxygens presented the highest productivity and selectivity for ethane ($453.20 \mu\text{mol g}^{-1} \text{h}^{-1}$ and 97.8%, respectively) in photocatalytic methane coupling reaction by involving trace amounts of water in a flow reactor. To

the best of our knowledge, this catalytic performance was the highest yield among the noble-metal free photocatalysts reported so far. Our comprehensive characterizations clearly revealed the origin of this high productivity and selectivity for ethane of NiMgAl-800. Firstly, the quasi-situ XPS and in-situ DRIFT analysis together demonstrated that the CH₄ molecules were activated on the surface oxygen sites of NiMgAl-800, highlighting the function of electron-enriched oxygen species in methane activation. DFT+U calculations illustrated the doping of Ni²⁺ ions would decrease the energy barrier for the dissociation of first C-H bond and promote the reactivity of NiMgAl-800. Secondly, the selectivity for ethane can be attributed to the H₂O molecules: the absorbed H₂O on the catalysts surface can modulate the Gibbs free energy of •CH₃ towards a coupling conductive pathway instead of over-oxidation, resulting in an increased C₂H₆ selectivity and the inhibition of over-oxidation to CO₂. This work offers an effective strategy on the rational design of noble-metal free catalysts for photocatalytic methane coupling reaction.

Methods

Chemicals. Ni(NO₃)₂·6H₂O (99%), Mg(NO₃)₂·6H₂O (99%), Al(NO₃)₃·6H₂O (99%), NaOH (>98%), Na₂CO₃ (>99%), NiO and MgO were obtained from Energy Chemistry and all the solvents were directly used without further purification. ¹²CH₄ and ¹³CH₄ (>99.999%) was purchased from Linde Gas Company.

Preparation of NiMgAl-LDH. The NiMgAl-LDH was synthesized through a traditional precipitation method. A mixed 20 mL aqueous solution composed of Ni²⁺ (1 mmol), Mg²⁺ (14 mmol), and Al³⁺ (5 mmol) ions was added drop by drop into an aqueous solution of Na₂CO₃ (20 mmol) and NaOH (20 mmol) with 20 mL deionized water via magnetic stirring. The reaction preparation temperature was carefully controlled at 80 °C. Once the synthesis finished, the product was collected immediately, centrifuged and washed with deionized water until pH = 7. Finally, the as-prepared NiMgAl-LDH was placed in a 60 °C vacuum oven overnight until completely dry (about 24 hours).

Synthesis of NiMgAl-x. The as-prepared NiMgAl-LDH were calcinated at different temperatures (200 °C, 400 °C, 600 °C, 800 °C and 1000 °C, respectively) in air for 3h. 200 mg of NiMgAl-LDH

was used for calcination was each time. Afterwards, the product NiMgAl-x was naturally cool to room temperature.

Photocatalytic methane coupling reaction. The photocatalytic methane coupling reaction was carried out in a home-made photocatalytic flow reactor equipped with a quartz window. In a typical test, 5 mg of as-prepared NiMgAl-x was spread evenly on the glass bowl and an amount of 300 μL water was put beneath the bowl. Firstly, the methane gas (>99.999%) was introduced to the reactor for 30 minutes with a flow rate of 20 mL min^{-1} . Then, the react system was irradiated under a 300 W Xe lamp (light intensity: 1.04 W cm^{-2}). The gas chromatograph with the equipment of TCD and FID detectors was used to analyze the produced gas products. The isotopic experiments was conducted in a bath reactor consist of 0.1 MPa CH_4 , 30 mg catalyst and 30 μL water with the substitution of $^{12}\text{CH}_4$ for $^{13}\text{CH}_4$ for 3h light irradiation. A gas GC-MS was utilized for product detection.

Computational details. All the calculations were performed with Vienna Ab initio Simulation Package. The generalized gradient approximation with the PW91 was utilized to correction interaction and describe exchange. Projector-augmented wave potentials were applied to elaborate the electron-ion interaction. The transition states were estimated with the climbing image nudged elastic band method, and checked by one imaginary frequency. The adsorption energy was calculated as follows: $E_{ads} = E_{X/slab} - E_{slab} - E_X$ where E_X is the energy of the free adsorbates in the gas phase. The barrier E_a and reaction energy E_r were calculated according to $E_a = E_{TS} - E_{IS}$ and $E_r = E_{FS} - E_{IS}$ in which E_{IS} , E_{FS} and E_{TS} represents the energy of initial state, final state, and transition state, respectively.

Data availability

All the data supporting the conclusions in research are available from the corresponding author for reasonable request.

References

1. E. McFarland. Unconventional Chemistry for Unconventional Natural Gas. *Science* **338**, 341-342 (2012).
2. Z. Chen, F. Zhang, B. Xu, Q. Zhang, J. Liu. Influence of methane content on a LNG heavy-duty engine with high compression ratio. *Energy* **128**, 329-336 (2017).
3. E. G. Nisbet, E. J. Dlugokencky, P. Bousquet. Methane on the Rise—Again. *Science* **343**, 493-495 (2014).
4. F. Schüth. Making more from methane. *Science* **363**, 1282-1283 (2019).
5. Z. Liu, F. Zhang, N. Rui, X. Li, L. Lin, L. E. Betancourt, D. Su, W. Xu, J. Cen, K. Attenkofer, H. Idriss, J. A. Rodriguez, S. D. Senanayake. Highly Active Ceria-Supported Ru Catalyst for the Dry Reforming of Methane: In Situ Identification of Ru^{δ+}-Ce³⁺ Interactions for Enhanced Conversion. *ACS Catal.* **9**, 3349-3359 (2019).
6. L. V. Mattos, G. Jacobs, B. H. Davis, F. B. B. Noronha. Production of Hydrogen from Ethanol: Review of Reaction Mechanism and Catalyst Deactivation. *Chem. Rev.* **112**, 4094-4123 (2012).
7. N. Levin, J. Lengyel, J. F. Eckhard, M. Tschurl, U. Heiz. Catalytic Non-Oxidative Coupling of Methane on Ta₈O₂⁺. *J. Am. Chem. Soc.* **142**, 5862-5869 (2020).
8. J. Shan, M. Li, L. F. Allard, S. Lee, M. Flytzani-Stephanopoulos. Mild oxidation of methane to methanol or acetic acid on supported isolated rhodium catalysts. *Nature* **551**, 605-608 (2017).
9. Z. Jin, L. Wang, E. Zuidema, K. Mondal, M. Zhang, J. Zhang, C. Wang, X. Meng, H. Yang, C. Mesters, F.-S. Xiao. Hydrophobic zeolite modification for in situ peroxide formation in methane oxidation to methanol. *Science* **367**, 193-197 (2020).
10. H. Song, X. Meng, Z.-J. Wang, H. Liu, J. Ye. Solar-Energy-Mediated Methane Conversion. *Joule* **3**, 1606-1636 (2019).
11. A. Hu, J.-J. Guo, H. Pan, Z. Zuo. Selective functionalization of methane, ethane, and higher alkanes by cerium photocatalysis. *Science* **361**, 668-672 (2018).
12. Z. Liang, T. Li, M. Kim, A. Asthagiri, J. F. Weaver. Low-temperature activation of methane on the IrO₂(110) surface. *Science* **356**, 299-303 (2017).
13. J. Lang, Y. Ma, X. Wu, Y. Jianga, Y. H. Hu. Highly efficient light-driven methane coupling under ambient conditions based on an integrated design of a photocatalytic system. *Green Chem.* **22**, (2020).
14. L. Luo, J. Luo, H. Li, F. Ren, Y. Zhang, A. Liu, W.-X. Li, J. Zeng. Water enables mild oxidation of methane to methanol on gold single-atom catalysts. *Nat. Commun.* **12**, 1218-1228 (2021).
15. X. Meng, X. Cui, N. P. Rajan, L. Yu, D. Deng, X. Bao. Direct Methane Conversion under Mild Condition by Thermo-, Electro-, or Photocatalysis. *Chem* **5**, 2296-2325 (2019).
16. X. Cui, H. Li, Y. Wang, Y. Hu, L. Hua, H. Li, X. Han, Q. Liu, F. Yang, L. He, X. Chen, Q. Li, J. Xiao, D. Deng, X. Bao. Room-Temperature Methane Conversion by Graphene-Confined Single Iron Atoms. *Chem* **4**, 1902-1910 (2018).
17. S. Wu, X. Tan, J. Lei, H. Chen, L. Wang, J. Zhang. Ga-Doped and Pt-Loaded Porous TiO₂-SiO₂ for Photocatalytic Nonoxidative Coupling of Methane. *J. Am. Chem. Soc.* **141**, 6592-6600 (2019).
18. X. Yu, V. L. Zholobenko, S. Moldovan, D. Hu, D. Wu, V. V. Ordonsky, A. Y. Khodakov. Stoichiometric methane conversion to ethane using photochemical looping at ambient temperature. *Nat. Energy* **5**, 511-519 (2020).
19. A. A. Latimer, A. R. Kulkarni, H. Aljama, J. H. Montoya, J. S. Yoo, C. Tsai, F. Abild-Pedersen, F. Studt, J. K. Nørskov. Understanding trends in C-H bond activation in heterogeneous catalysis. *Nat. Mater.* **16**, 225-230 (2017).

-
20. X. Li, J. Xie, H. Rao, C. Wang, J. Tang. Platinum- and CuO_x-Decorated TiO₂ Photocatalyst for Oxidative Coupling of Methane to C₂ Hydrocarbons in a Flow Reactor. *Angew. Chem. Int. Ed.* **59**, 19702-19707 (2020).
21. S. Song, H. Song, L. Li, S. Wang, W. Chu, K. Peng, X. Meng, Q. Wang, B. Deng, Q. Liu, Z. Wang, Y. Weng, H. Hu, H. Lin, T. Kako, J. Ye. A selective Au-ZnO/TiO₂ hybrid photocatalyst for oxidative coupling of methane to ethane with dioxygen. *Nature Catalysis* **4**, 1032-1042 (2021).
22. G. Wang, X. Mu, J. Li, Q. Zhan, Y. Qian, X. Mu, L. Li. Light-Induced Nonoxidative Coupling of Methane Using Stable Solid Solutions. *Angew. Chem. Int. Ed.* **60**, 20760-20764 (2021).
23. Z. Zuo, S. Liu, Z. Wang, C. Liu, W. Huang, J. Huang, P. Liu. Dry Reforming of Methane on Single-Site Ni/MgO Catalysts: Importance of Site Confinement. *ACS Catal.* **8**, 9821-9835 (2018).
24. F. Cheng, X. Duan, K. Xie. Dry Reforming of CH₄/CO₂ by Stable Ni Nanocrystals on Porous Single-Crystalline MgO Monoliths at Reduced Temperature. *Angew. Chem. Int. Ed.* **60**, 2-10 (2021).
25. Y. Xu, X. Sun, X. Wang, L. He, M. T. Wharmby, X. Hua, Y. Zhao, Y.-F. Song. Topological Transformation of Mg-Containing Layered Double Hydroxide Nanosheets for Efficient Photodriven CH₄ Coupling. *Chem. Eur. J* **27**, 13211-13220 (2021).
26. P. Schwach, M. G. Willingel, A. Trunschke, R. Schlögl. Methane Coupling over Magnesium Oxide: How Doping Can Work. *Angew. Chem. Int. Ed.* **52**, 11381-11384 (2013).
27. L. Tan, S.-M. Xu, Z. Wang, Y. Xu, X. Wang, X. Hao, S. Bai, C. Ning, Y. Wang, W. Zhang, Y. K. Jo, S.-J. Hwang, X. Cao, X. Zheng, H. Yan, Y. Zhao, H. Duan, Y.-F. Song. Highly Selective Photoreduction of CO₂ with Suppressing H₂ Evolution over Monolayer Layered Double Hydroxide under Irradiation above 600 nm. *Angew. Chem. Int. Ed.* **58**, 11860-11867 (2019).
28. S. Bai, T. Li, H. Wang, L. Tan, Y. Zhao, Y.-F. Song. Scale-up synthesis of monolayer layered double hydroxide nanosheets via separate nucleation and aging steps method for efficient CO₂ photoreduction. *Chem. Eng. J.* **419**, 129390-129398 (2021).
29. C. Ning, Z. Wang, S. Bai, L. Tan, H. Dong, Y. Xu, X. Hao, T. Shen, J. Zhao, P. Zhao, Z. Li, Y. Zhao, Y.-F. Song. 650 nm-driven syngas evolution from photocatalytic CO₂ reduction over Co-containing ternary layered double hydroxide nanosheets. *Chem. Eng. J.* **412**, 128362-128370 (2021).
30. Z. Wang, S.-M. Xu, Y. Xu, L. Tan, X. Wang, Y. Zhao, H. Duan, Y.-F. Song. Single Ru atoms with precise coordination on a monolayer layered double hydroxide for efficient electrooxidation catalysis. *Chem. Sci.* **10**, 378-384 (2019).
31. G. Liu, Z. Wang, T. Shen, X. Zheng, Y. Zhao, Y.-F. Song. Atomically dispersed Rh-doped NiFe layered double hydroxides: precise location of Rh and promoting hydrazine electrooxidation properties. *Nanoscale* **13**, 1869-1874 (2021).
32. Y. Zhao, X. Jia, G. Chen, L. Shang, G. I. N. Waterhouse, L.-Z. Wu, C.-H. Tung, D. O'hare, T. Zhang. Ultrafine NiO Nanosheets Stabilized by TiO₂ from Monolayer NiTi-LDH Precursors: An Active Water Oxidation Electrocatalyst. *J. Am. Chem. Soc.* **138**, 6517-6524 (2016).
33. Y. Zhao, B. Zhao, J. Liu, G. Chen, R. Gao, S. Yao, M. Li, Q. Zhang, L. Gu, J. Xie, X. Wen, L.-Z. Wu, C.-H. Tung, D. Ma, T. Zhang. Oxide-Modified Nickel Photocatalyst for the Production of Hydrocarbons in Visible Light. *Angew. Chem. Int. Ed.* **55**, 4215-4219 (2016).
34. L. Tan, S.-M. Xu, Z. Wang, X. Hao, T. Li, H. Yan, W. Zhang, Y. Zhao, Y.-F. Song. 600 nm induced nearly 99% selectivity of CH₄ from CO₂ photoreduction using defect-rich monolayer structures. *Cell Rep. Phys. Sci.* **2**, 100322-100338 (2021).

-
35. Z. Wang, S.-M. Xu, L. Tan, G. Liu, T. Shen, C. Yu, H. Wang, Y. Tao, X. Cao, Y. Zhao, Y.-F. Song. 600 nm-driven photoreduction of CO₂ through the topological transformation of layered double hydroxides nanosheets. *Appl. Catal. B: Environ.* **270**, 118884-118883 (2020).
36. Y. Xu, Z. Wang, L. Tan, Y. Zhao, H. Duan, Y.-F. Song. Fine Tuning the Heterostructured Interfaces by Topological Transformation of Layered Double Hydroxide Nanosheets. *Ind. Eng. Chem. Res.* **57**, 10411-10420 (2018).
37. Y. Xu, Z. Wang, L. Tan, H. Yan, Y. Zhao, H. Duan, Y.-F. Song. Interface Engineering of High-Energy Faceted Co₃O₄/ZnO Heterostructured Catalysts Derived from Layered Double Hydroxide Nanosheets. *Ind. Eng. Chem. Res.* **57**, 5259-5267 (2018).
38. B. L. Farrell, V. O. Igenegbai, S. Linic. A Viewpoint on Direct Methane Conversion to Ethane and Ethylene Using Oxidative Coupling on Solid Catalysts. *ACS Catal.* **6**, 4340-4346 (2016).
39. S. Ardizzone, C. L. Bianchi, M. Fadoni, B. Vercelli. Magnesium salts and oxide: an XPS overview. *Appl. Surf. Sci.* **119**, 253-259 (1997).
40. B. L. Mojet, S. D. Ebbesen, L. Lefferts. Light at the interface: the potential of attenuated total reflection infrared spectroscopy for understanding heterogeneous catalysis in water. *Chem. Soc. Rev.* **39**, 4643-4655 (2010).

Acknowledgements

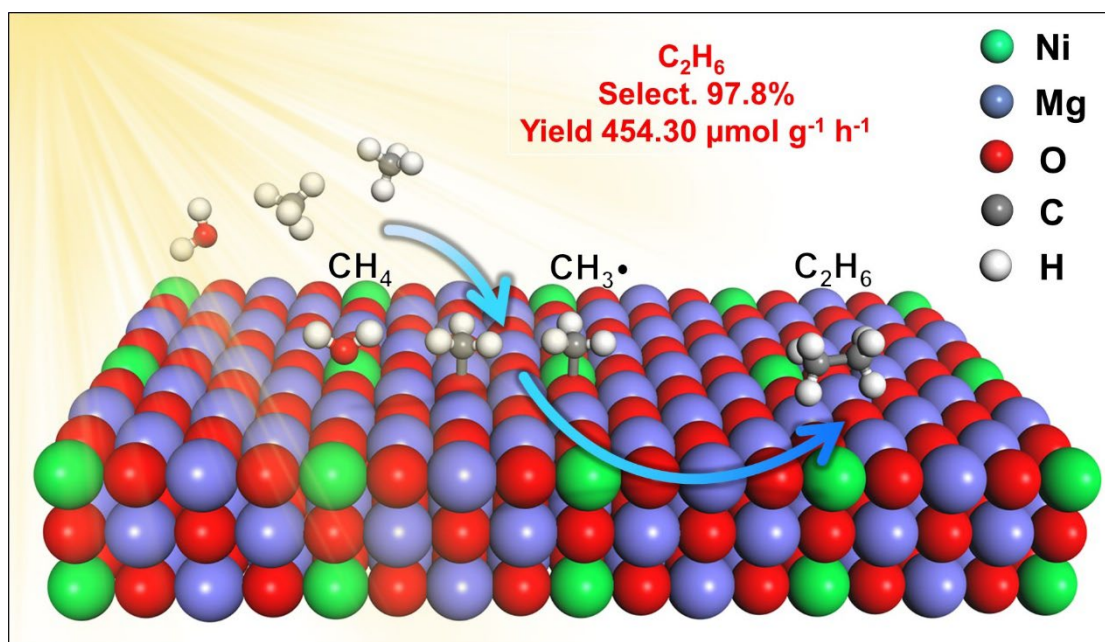
This research was supported by the National Nature Science Foundation of China (22178019, U1707603, 21625101) and the Fundamental Research Funds for the Central Universities (XK1802-6, XK1803-05, XK1902, 12060093063). The XAFS experiments were conducted in 1W1B beamline of the Beijing Synchrotron Radiation Facility.

Author contributions

Tianyang Shen synthesized the catalyst, conducted the photocatalytic methane coupling reaction experiments, performed all the characterization analysis. Ya Bai performed the DFT+U calculations. Zelin Wang contributed to the discussion on this work and gave lots of meaningful suggestions. Guihao Liu, Xiaoliang Sun were helpful in the XAFS analysis and optimization of reaction conditions. Jiaxin Li and Sha Bai repeat the photocatalytic experiment to ensure that the experimental results are reproducible. Lirong Zheng helped supervise the XAFS analysis. Yu-Fei Song designed the study, supervised all the experiments.

Competing interests

The authors declare no competing interests.



By involving trace amounts of water, NiMgAl-800 presented a high production rate and a superior selectivity for ethane ($454.30 \mu\text{mol g}^{-1} \text{h}^{-1}$ and 97.8%, respectively) in the photocatalytic methane coupling reaction, which is the highest yield among the noble-metal free photocatalysts reported so far. Such high reactivity and selectivity can be attributed to the isomorphous doped Ni^{2+} ions, the electron-enriched surface oxygen species and the introduced water that can modulate the Gibbs free energy of $\bullet\text{CH}_3$ towards a coupling conductive pathway, respectively.

Supplementary Files

This is a list of supplementary files associated with this preprint. Click to download.

- [15SupplementaryInformationNiMgAlxTY.docx](#)